Research Repository UCD

Provided by the author(s) and University College Dublin Library in accordance with publisher policies. Please cite the published version when available.

Title	Highly Efficient Broadband Continuous Inverse Class-F Power Amplifier Design Using Modified Elliptic Low-Pass Filtering Matching Network
Authors(s)	Yang, Mengsu; Xia, Jing; Guo, Yan; Zhu, Anding
Publication date	2016-05
Publication information	IEEE Transactions on Microwave Theory and Techniques, 64 (5): 1515-1525
Publisher	IEEE
Item record/more information	http://hdl.handle.net/10197/8388
Publisher's statement	© 2016 IEEE. Personal use of this material is permitted. Permission from IEEE must be obtained for all other uses, in any current or future media, including reprinting/republishing this material for advertising or promotional purposes, creating new collective works, for resale or redistribution to servers or lists, or reuse of any copyrighted component of this work in other works.
Publisher's version (DOI)	10.1109/TMTT.2016.2544318

Downloaded 2022-08-20T16:25:46Z

The UCD community has made this article openly available. Please share how this access benefits you. Your story matters! (@ucd_oa)

Highly Efficient Broadband Continuous Inverse Class-F Power Amplifier Design Using Modified Elliptic Low-Pass Filtering Matching Network

Mengsu Yang, Jing Xia, *Member, IEEE*, Yan Guo, *Student Member*, *IEEE,* and Anding Zhu, *Senior Member*, *IEEE*

***Abstract*— This paper proposes a design approach for a broadband and high efficiency continuous inverse Class-F (CCF^{-1}) power amplifier (PA) based on a modified elliptic low-pass filtering (LPF) matching network (MN). From theoretical and practical perspectives, the importance of a swift impedance transition from the higher end of the fundamental frequency band to the lower end of the second harmonic band is discussed, when designing a broadband, single-mode PA. After being compared with widely used Chebyshev LPF MNs, a modified elliptic LPF MN, which provides a sharp roll-off, is utilized to provide the required rapid transition. A step-by-step design procedure of the proposed modified elliptic LPF MN is presented. Experimental results show that a high efficiency CCF^{-1} PA is realized from 1.35 to 2.5 GHz (fractional bandwidth = 60%) with measured drain efficiency of 68%-82% and output power of 41.1-42.5 dBm. When stimulated by a 20-MHz LTE signal with an average output power of approximately 34.5 dBm, the proposed PA, combined with digital pre-distortion, achieved adjacent channel leakage ratios below -45 dBc, with average efficiency ranging from 37% to 45.8%. Similar performance is measured when the proposed PA is driven by a dual-band, dual-mode modulated signal with a 100-MHz instantaneous bandwidth at a center frequency of 2.14 GHz.**

***Index Terms*— Broadband amplifiers, digital predistortion (DPD), high efficiency, low-pass matching network, power amplifier (PA), wideband microwave amplifiers.**

I. Introduction

THE consistent demands for high performance and high data rates, with reduced cost and power consumption, impose significant challenges in radio frequency (RF) power amplifier (PA) design for wireless communications. The Class-J PA, first presented by Cripps [1], offers a wide range of high performance solutions that can be obtained over a wide bandwidth by allowing a reactive component at the fundamental and reactive terminations at the harmonics [2]. This principle was then extended to both the Class-F and inverse Class-F modes [3]-[6], in the form of the continuous Class-F (CCF) and continuous inverse Class-F (CCF^{-1}) modes, respectively. The advantage of such advanced PA modes is that high efficiency amplifications can be achieved across wide bandwidth because stringent harmonic impedance requirements are alleviated.

In practice, realization of these modes requires proper matching at both the fundamental and the harmonics. To date, many impedance matching techniques have been thoroughly explored. In particular, multistage, low-pass topologies are often utilized for this task [7]-[15]. For instance, a synthesized Chebyshev low-pass filtering (LPF) matching network (MN) based on series transmission-lines and open-circuit stubs were used in a highly efficient broadband Class-E PA [8]. In [14], the simplified frequency technique was employed to design a broadband CCF PA implemented with commensurate stepped-impedance transmission-line. Nevertheless, such broadband matching techniques run into difficulty when the bandwidth of interest approaches an octave. In principle, the desired fundamental and second harmonic impedances are normally located in different regions of the Smith chart. In a wideband design, e.g., for an octave bandwidth, however, the highest frequency of the desired band (f_H) will be very close to the second harmonic of the lowest frequency of the band ($2f_L$). If traditional matching techniques are employed, the impedance values at f_H and $2f_L$ will be similar because of the smooth transitions in the roll off region, which violates the load impedance requirement for the CCF or CCF^{-1} modes, and thus the system performance is degraded.

To resolve the aforementioned issue, in this paper, the characteristics of elliptic low-pass filters [16] is proposed to be explored in the design of the output matching network (OMN) for a CCF^{-1} PA. The proposed OMN could offer rapid transition from f_H to $2f_L$ and thus simultaneously obtain optimum matching at the fundamental and the second harmonic. The concept is first introduced in comparison with the conventional Chebyshev low-pass filters. A synthesized approach for microstrip realization of the modified elliptic LPF MN is presented, starting from a lumped-elements prototype. For the purpose of validation, a broadband and highly-efficient PA operating in the CCF^{-1} mode is designed, implemented, and measured.

This paper is organized as follows. Section II analyzes the theoretical impedance distribution of the CCF^{-1} PA mode, revealing the importance of swift transition between f_H and $2f_L$ for bandwidth extension, and finally proposes to employ the

This work was supported by the China Scholarship Council and in part by the Science Foundation Ireland under Grant Numbers 13/RC/2077 and 12/IA/1267.

The authors are with the School of Electrical and Electronic Engineering, U niversity College Dublin, Dublin 4, Ireland (e-mail: mengsu.yang@ucdconnect.ie, jing.xia@ucd.ie, yan.guo.1@ucdconnect.ie, anding.zhu@ucd.ie).

characteristics of an elliptic low-pass filter as a promising solution. In Section III, after identifying the optimum fundamental and second harmonic loads in both theoretical and experimental ways, the comprehensive design procedure of the proposed modified elliptic LPF OMN is described in detail. In Section IV, the proposed PA is tested with a continuous-wave (CW) signal, revealing greater than 68% drain efficiency (DE), with at least 41.1 dBm of output power from 1.35 GHz to 2.5 GHz. Moreover, the potential of the proposed PA, when combined with digital pre-distortion (DPD) techniques, to linearly amplify modulated signals under various scenarios is validated at different frequencies in the section. Conclusions are presented in Section V.

II. Broadband Output Matching Network for Continuous Inverse Class-F PAs

A. Standard Continuous Inverse Class-F PA Mode

The standard CCF^{-1} PA mode, which originates from the inverse Class-F PA mode, presents a half-wave rectified sinusoidal voltage waveform $v(\theta)$ at the intrinsic current-generator plane of the device [6]:

$$v(\theta) = 1 + \frac{2}{\sqrt{2}}\cos\theta + \frac{1}{2}\cos 2\theta, \tag{1}$$

while the current waveform $i(\theta)$ is no longer rigorously restrained to a square waveform but includes a set of variations dependent upon the parameter γ [5],

$$i(\theta) = (i_{DC} - i_1\cos\theta + i_3\cos 3\theta)\cdot(1 - \gamma\sin\theta) \tag{2}$$

where i_{DC}=0.37, i_1=0.43, and i_3=0.06. The fundamental, the second and the third harmonic loads of the CCF^{-1} PA can be expressed in the form of admittance as

$$Y_{1,CCF^{-1}} = G_{opt}\sqrt{2}i_1 + jG_{opt}\sqrt{2}i_{DC}\gamma \tag{3}$$

$$Y_{2,CCF^{-1}} = -jG_{opt}2(i_1 + i_3)\gamma \tag{4}$$

$$Y_{3,CCF^{-1}} = \infty \tag{5}$$

where $G_{opt}=1/R_{opt}=0.5\cdot I_{max}/(V_{DC}-V_{knee})$ and γ is used to tune the voltage and current waveforms at different frequencies over a desired bandwidth. As illustrated in Fig. 1, the fundamental impedance is located towards the center of the Smith chart while the second harmonic impedance is on the edge of Smith chart and the third harmonic presents a short circuit.

B. Bandwidth of the Continuous Inverse Class-F PA Mode

Although the CCF^{-1} mode can enable highly-efficient amplification over a wide bandwidth, it encounters difficulties in maintaining this mode when the bandwidth of interest grows

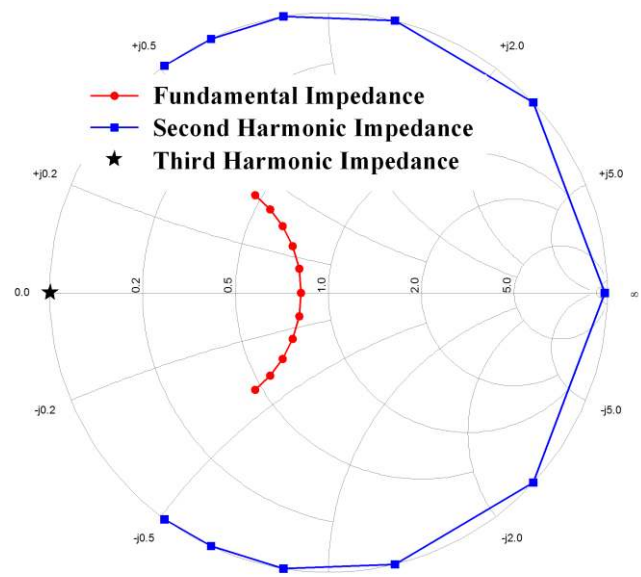

Fig. 1. Theoretical fundamental, second harmonic, and third harmonic impedance of CCF^{-1} PA mode.

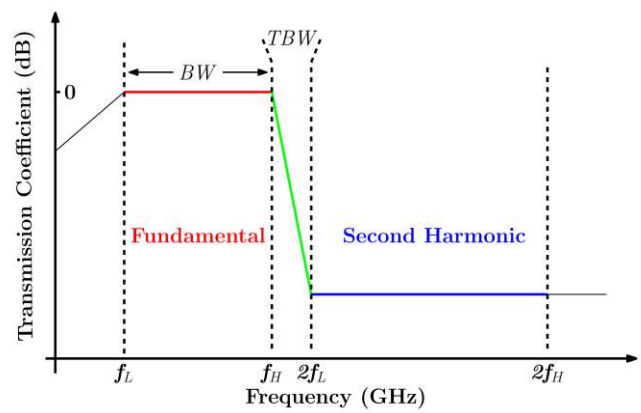

Fig. 2. Expected frequency response of a broadband CCF^{-1} PA.

towards an octave, representing a fractional bandwidth of 66%. Fig. 2 demonstrates the frequency band distribution of a broadband CCF^{-1} PA. Let's assume the fundamental band ranges from f_L to f_H, which results in a second harmonic zone from $2f_L$ to $2f_H$. If the bandwidth of the fundamental band is defined as BW, and that of the transition band between the fundamental band and the second harmonic band as TBW, the following equations are obtained,

$$BW = f_H - f_L \tag{6}$$

$$TBW = 2f_L - f_H \tag{7}$$

Clearly, it can be seen that any increment of BW would necessarily result in the decrease of TBW since their sum is fixed.

For a CCF^{-1} PA, the fundamental admittance cannot be equal to the second harmonic admittance, because (3) contains a real

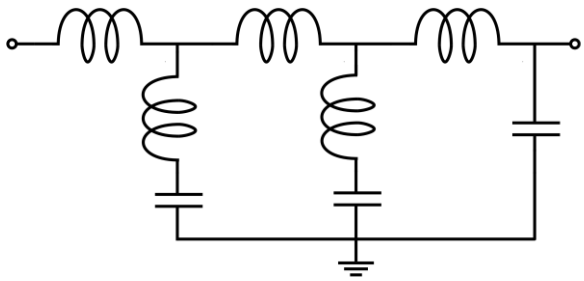

Fig. 3. LC prototype of a 6th-order elliptic low-pass filter.

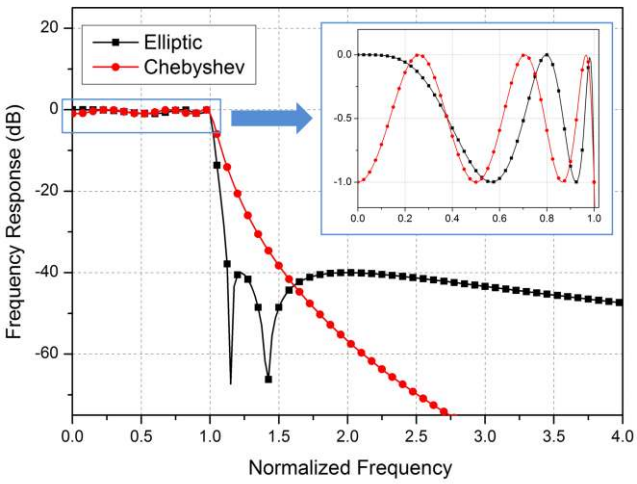

Fig. 4. Frequency response comparison between elliptic low-pass filter and Chebyshev low-pass filter with the same filter order of 6.

part while (4) does not. For a passive MN, it is impossible to transform a load to two different admittances at a single frequency point. Hence, to maintain the CCF^{-1} mode, TBW must be greater than zero and be minimized as much as possible to maximize the bandwidth BW. To do so, an OMN that can have a dramatic change in impedance in the transition region is in demand so that a sudden conversion can be made to move the impedance from the inner region to the edge of the Smith chart. In practice, however, it is difficult to design such OMNs. For instance, the widely used Chebyshev LPF MNs [8]-[10] are capable of providing accurate fundamental matching over wide bandwidth and purely reactive termination at harmonics but they require a large TBW because the transition from passband to stopband is gradual, which limits the bandwidth extension.

C. *Elliptic Low-Pass Filter*

The elliptic low-pass filter, also known as an elliptic-function low-pass filter, is characterized by a passband ripple of equal amplitude as well as a stopband ripple of equal amplitude [16]. An elliptic filter is capable of providing attenuation poles at specific frequencies which brings a very sharp rate of cutoff. The generation of attenuation poles can be obtained by introducing series-resonant branches connected in shunt that short out transmission at the resonant frequencies. In Fig. 3, the

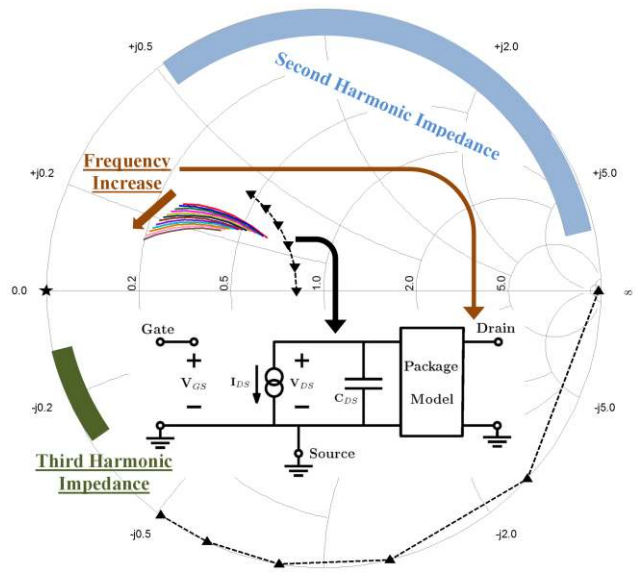

Fig. 5. Theoretical fundamental, second harmonic, and third harmonic impedance at the intrinsic current generator plane and the package plane.

prototype of a 6th-order elliptic filter which is composed of inductors and capacitors is displayed. In comparison with other types of low-pass filters, e.g., Chebyshev filters, elliptic filters offer a faster transition from the passband to the stopband, as illustrated in Fig. 4. Furthermore, the influence of the passband ripples is negligible because their amplitudes are too small to significantly affect the fundamental impedance seen by the device. Similarly, ripples in the stopband have little impact because the magnitude of loss is very large. In summary, the characteristics of elliptic low-pass filters largely satisfy the requirements discussed above for designing a broadband OMN that has a fast transition between the passband and stopband. In this work, an elliptic filter structure is proposed to be employed as the OMN for the CCF^{-1} PA.

III. Design of Broadband Continuous Inverse Class-F PAs Based On Modified Elliptic Low-Pass Filtering Matching Network

A. *Optimum Load Impedance Analysis*

In this work, our objective is to design a high efficiency (>70%) and high output power (>41 dBm) PA from 1.4 GHz to 2.5 GHz. As a result, a 10 W GaN HEMT from Cree (CGH40010F) was picked. Following the analysis of Section II, the desired fundamental and harmonic load impedances at the intrinsic current generator plane were determined, as shown in Fig. 5 with black dotted lines and pentagram. Since there is no need to explore the whole range of γ, it was settled in the range from 0 to 1, which represents the upper half of the theoretical fundamental impedance range. Subsequently, the corresponding second harmonic impedance is located in the lower half of the Smith chart.

When dealing with a realistic packaged transistor, the

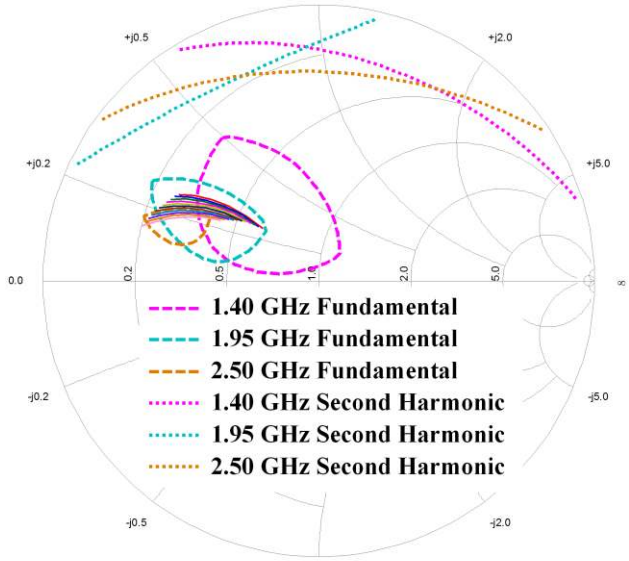

Fig. 6. Merged output power and efficiency contours (efficiency≥70%, output power≥41dBm) for fundamental impedance extracted from the load-pull simulation, and optimum region for second harmonic impedance (efficiency degradation less than 2%).

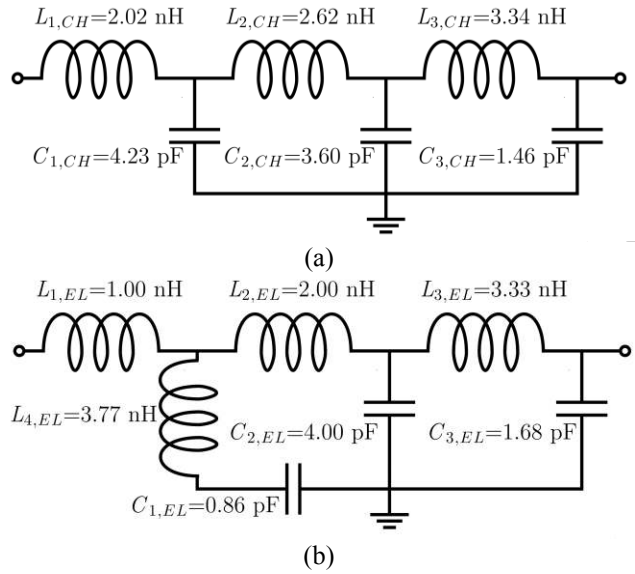

Fig. 7. LC prototypes. (a) Prototype of Chebyshev LPF MN. (b) Prototype of modified elliptic LPF MN.

theoretical impedance at the intrinsic current generator plane should be converted to that at the package plane. By employing the approximate parasitic model extracted from [17], the fundamental impedance at the package plane from 1.4 to 2.5 GHz with a step of 100 MHz can be assessed, as displayed in Fig. 5. It can be observed that, with the rise of frequency, the fundamental impedance trajectories are represented by a set of colored curves slowly moving to the left side with a counterclockwise rotation. Meanwhile, the optimum second harmonic impedance at the package plane is located at the top right margin of the Smith chart. Moreover, the third harmonic impedance holds a reactance that roughly ranges from -15 Ω to -5 Ω.

Because the analysis presented above was based on theory and the approximate parasitic model, its deviation from the real device must be examined so as to eliminate any possible inaccuracy. Thus, to validate the effectiveness of the theoretical impedance derivation and to further improve performance, load-pull simulations with a large signal model of the same device were carried out in ADS2013, as illustrated in Fig. 6. It was found that the optimum fundamental and second harmonic impedance obtained from simulation approximately matched those derived from theory, while the third harmonic impedance shows trivial influence. Hence, by ignoring the third harmonic impedance, the design of the OMN is simplified to the fundamental and the second harmonic matching.

B. Realization of Broadband Modified Elliptic Low-Pass Filtering Matching Network

So far, the topology and the target impedance of the OMN have been determined. The next step is the realization. In this design, the swift transition is only required between f_H and $2f_L$, which can be satisfied by using only one attenuation pole that is set at $f_p = 2f_L = 2.8$ GHz. In fact, using more attenuation poles can further suppress the second harmonic, but it will increase the design complexity.

The standard elliptic low-pass filter does not provide an impedance transformation. In this work, a synthesis methodology to design a modified elliptic LPF MN that is capable of providing the desired impedance transformation is presented in the following. The design procedure includes three main steps as described below.

Firstly, according to the required impedance transformation ratio and fractional bandwidth, a real-to-complex Chebyshev LPF MN can be generated and optimized by utilizing the process illustrated in [8], as shown in Fig. 7(a).

Secondly, the first shunt capacitor $C_{1,CH}$ in the Chebyshev LPF MN is replaced with a series-resonant branch, shown in Fig 7(b). This particular resonator is responsible for the generation of the attenuation pole f_p. In addition, this resonator is expected to show similar behavior as the capacitor $C_{1,CH}$ does at the cutoff frequency f_H. Thus, $L_{4,EL}$ and $C_{1,EL}$ in the modified elliptic LPF MN can be determined by f_p, f_H and $C_{1,CH}$

$$L_{4,EL} = \frac{1}{C_{1,CH} \cdot \left[\left(2\pi f_p\right)^2 - \left(2\pi f_H\right)^2 \right]} \tag{8}$$

$$C_{1,EL} = \frac{\left[\left(2\pi f_p\right)^2 - \left(2\pi f_H\right)^2 \right]}{\left(2\pi f_p\right)^2} \cdot C_{1,CH} \tag{9}$$

The values of the other lumped elements can be obtained via post-optimization to achieve the in-band matching without affecting the predetermined attenuation pole.

Fig. 8(a) demonstrates the frequency response of the

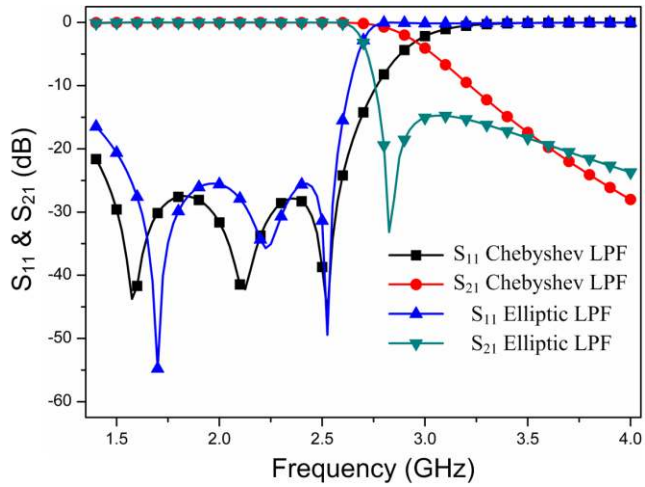

(a)

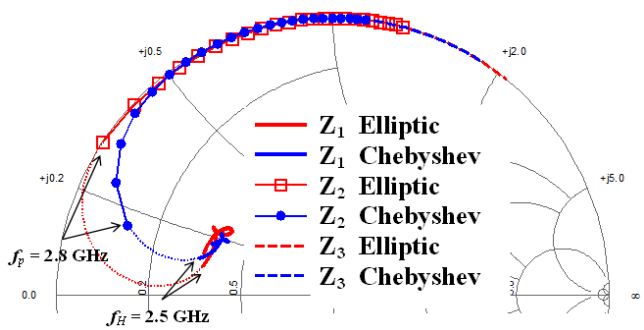

(b)

Fig. 8. Comparison between modified elliptic and Chebyshev LPF MNs. (a) Forward transfer function S_{21} and input return loss S_{11}. (b) Impedance trajectories from the fundamental to the third harmonic.

proposed MN and the Chebyshev MN, in terms of forward transfer functions S_{21} and input return losses S_{11}. As can be seen, the elliptic MN provides a sudden drop in S_{21} at 2.6 GHz, which corresponds to the attenuation pole, while the S_{21} of the Chebyshev MN has a smooth roll-off. On the other hand, the S_{11} of the former does not show significant degradation compared with that of the latter. The impedance trajectories from the fundamental to the third harmonic of the elliptic LPF MN and the Chebyshev LPF MN are displayed in Fig. 8(b). As expected, the fundamental impedance of the modified elliptic LPF MN is appropriately allocated and largely overlapped with that of the latter. More importantly, the second harmonic impedance of the former is kept to the side of Smith chart, while the latter can't do the same at the lower end of the second harmonic. It indicates that the proposed MN can realize the desired swift impedance transition from f_H to $2f_L$ while the Chebyshev MN cannot.

Finally, when all the lumped elements are determined, the transformation to distributed elements can be undertaken as follows. In this design, a Taconic RF35 substrate with a relative dielectric constant of 3.5 and a thickness of 1.52 mm was chosen for the microstrip realization. Those lumped elements were converted by replacing inductors and capacitors with

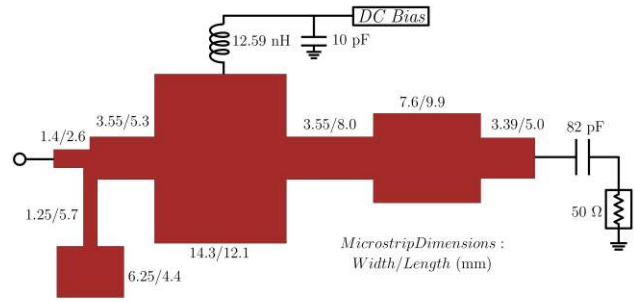

Fig. 9. Layout of modified elliptic LPF OMN.

high-impedance microstrip lines and low-impedance microstrip lines, respectively. Since the width of microstrip line is correlated with its characteristic impedance, which had already been selected according to the feasibility and convenience of implementation, the corresponding physical length of each element can be solved. Furthermore, to achieve a more accurate design, compensations are necessary for unwanted effects introduced by the microstrip lines and discontinuities according to [18]. For instance, regarding capacitive element C_i, influences from its adjacent inductive elements L_{left} and L_{right} should be taken into account for the correction. Inductive elements are treated in a similar manner. Generally speaking, the corrected physical lengths of those microstrip elements should satisfy the following equations at the cutoff frequency f_H

$$2\pi f_H C_i = \frac{1}{Z_{C_i}}\sin\left(\frac{2\pi l_{C_i}}{\lambda_{gC_i}}\right) + \frac{1}{Z_{L_{left}}}\tan\left(\frac{\pi l_{L_{left}}}{\lambda_{gL_{left}}}\right) + \frac{1}{Z_{L_{right}}}\tan\left(\frac{\pi l_{L_{right}}}{\lambda_{gL_{right}}}\right). \tag{10}$$

$$2\pi f_H L_i = Z_{L_i}\sin\left(\frac{2\pi l_{L_i}}{\lambda_{gL_i}}\right) + Z_{C_{left}}\tan\left(\frac{\pi l_{C_{left}}}{\lambda_{gC_{left}}}\right) + Z_{C_{right}}\tan\left(\frac{\pi l_{C_{right}}}{\lambda_{gC_{right}}}\right). \tag{11}$$

where Z_{Ci} and Z_{Li} are the characteristic impedance of the conductive and inductive elements, and λ_{gCi} and λ_{gLi} are the corresponding guided wavelength.

By following the procedure described above, a broadband OMN based on the modified elliptic LPF MN was designed and realized with microstrip, as displayed in Fig. 9. Fig. 10 demonstrates the simulated impedance presented by the proposed OMN at the package plane and the intrinsic current generator plane. As can be seen from Fig. 10(a), the fundamental impedance lies inside the optimum region acquired from the load-pull, while the second harmonic impedance spreads at the top edge of Smith chart, which meets the requirement shown in Fig. 6. It can be found from Fig. 10(b) that both the fundamental and the second harmonic impedances largely overlap with the corresponding theoretical impedances

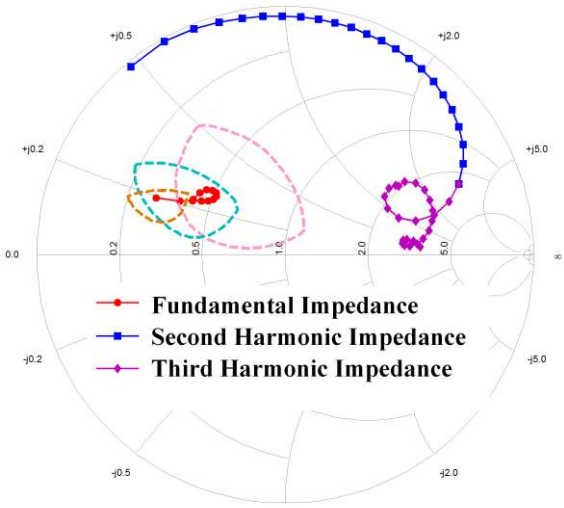

(a)

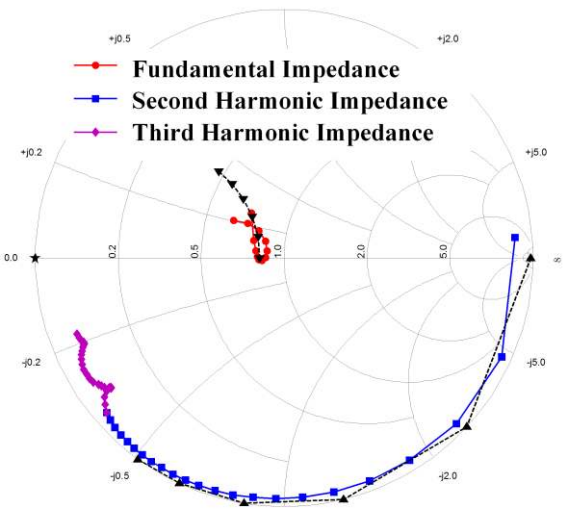

(b)

Fig. 10. Load impedance presented by modified elliptic LPF OMN at the package plane (a) and the intrinsic current generator plane (b), respectively.

which are shown as downwards and upwards black triangle dash lines, respectively. The third harmonic impedance converges on the capacitive part near the short circuit point, which is considered as a proper approximation to the ideal short termination.

C. Realization of a Broadband Input Matching Network

Regarding the design of the input matching network (IMN), the conventional Chebyshev LPF MN can be employed because of the following two reasons. First of all, unlike the output harmonic impedances, those of the input play a less critical role in efficiency enhancement. Thus, the fundamental source impedance is the priority and the second harmonic impedance can be neglected when designing the IMN.

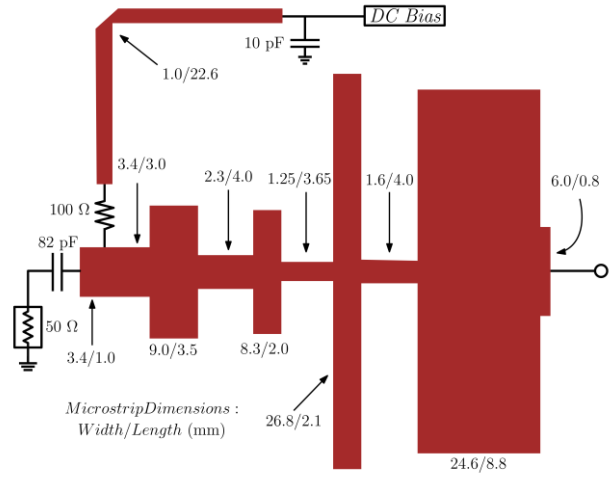

Fig. 11. Layout of 8th-order Chebyshev IMN.

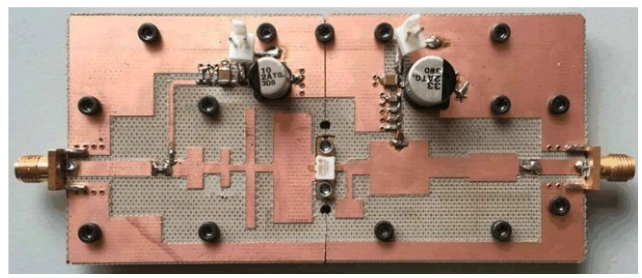

Fig. 12. Fabricated PA using modified elliptic LPF OMN.

Secondly, for this specific 10 W transistor, its fundamental source impedance has a very small real part around 5 Ω over the band of interest, which gives rise to a large impedance transformation ratio. Hence, to guarantee a precise impedance matching across the band of interest, an 8th-order Chebyshev LPF MN was employed as the IMN of the proposed PA, as displayed in Fig. 11.

IV. Implementation and Measurements

To verify the proposed approach, a broadband PA was fabricated as shown in Fig. 12. By employing Cree's six-port large signal model, it is possible to study the intrinsic waveforms in ADS prior to measurement. Fig. 13(a)-(c) show the simulated voltage and current waveforms at the intrinsic current generator plane, when the proposed PA was stimulated by CW signals at 1.5, 2.0, and 2.5 GHz, respectively. As can be seen from Fig. 13(a), the proposed PA generates a standard inverse Class-F mode waveform at 1.5 GHz with a half-sinusoidal voltage and a square-wave current. At 2.0 GHz and 2.5 GHz, the current waveforms were slightly differed from the ideal one but still conformed to the family of the CCF^{-1} mode waveform.

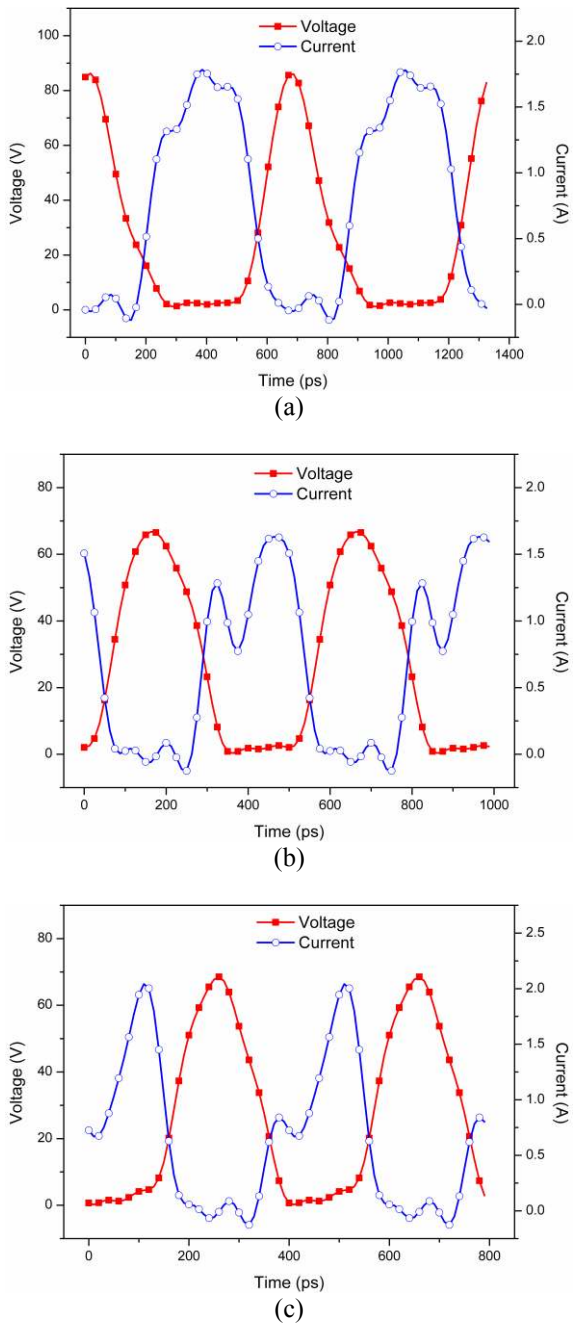

Fig. 13. Intrinsic voltage and current waveforms. (a) at 1.5 GHz. (b) at 2.0 GHz. (c) at 2.5 GHz.

To evaluate the performance of the implemented PA for various applications, different types of measurements were carried out as follows.

A. Measurement Results with CW Signal

At first, a CW signal was employed as the stimulus to the proposed PA from 1.35 to 2.5 GHz. Fig. 14 depicts the measurement results, in terms of drain efficiency and output power, as well as the simulated results. It can be seen that the DE maintained higher than 68% between 1.35 GHz and 2.5 GHz giving a fractional bandwidth of 60%. The maximum DE of 82% was measured at 1.6 GHz. In general, the output power remained in the range of 41.1 dBm to 42.5 dBm over the entire desired band.

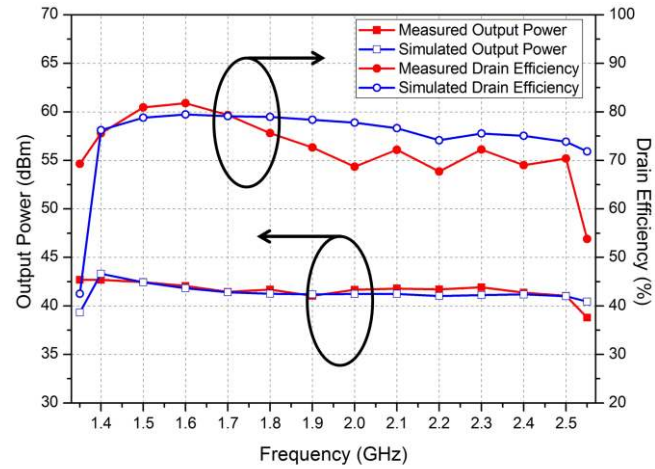

Fig. 14. Measured and simulated output power and DE versus frequency from 1.35 to 2.55 GHz.

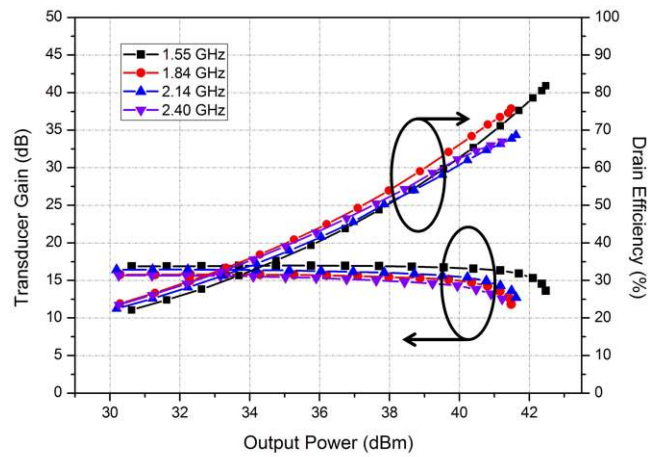

Fig. 15. Measured gain and DE versus output power at 1.55, 1.84, 2.14, and 2.4 GHz, respectively.

TABLE I
Broadband PAs Comparison with CW Signal

Ref	BW (GHz)/(%)	Gain (dB)	Power (W)	DE (%)
[7]	1.9-4.3/78	9-11	10-15	57-72
[9]	1.3-3.3/87	10-13	10-11	60-83
[10]	2-3.5/54.5	≈13	11.2-16	64-76
[13]	1.7-2.8/49	14.4-15.3	10.5-19.5	61-81
[14]	1.45-2.45/51	10-12.6	11-16.6	70-81
[15]	0.9-3.2/112	10-14	9-20	52-85*
This Work	1.35-2.5/60	15.2-17	12.5-18	68-82

*Only power-added efficiency was provided in [17].

The measured DE and gain versus output power at four commercially-used frequency bands (1.55, 1.84, 2.14 and 2.40

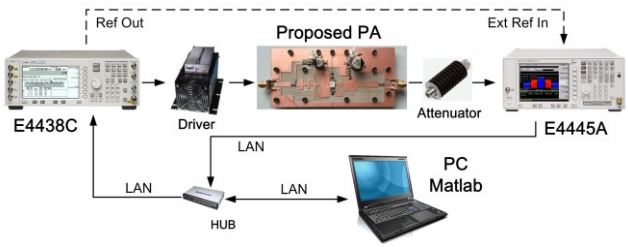

Fig. 16. Linearization platform for 20-MHz LTE signal.

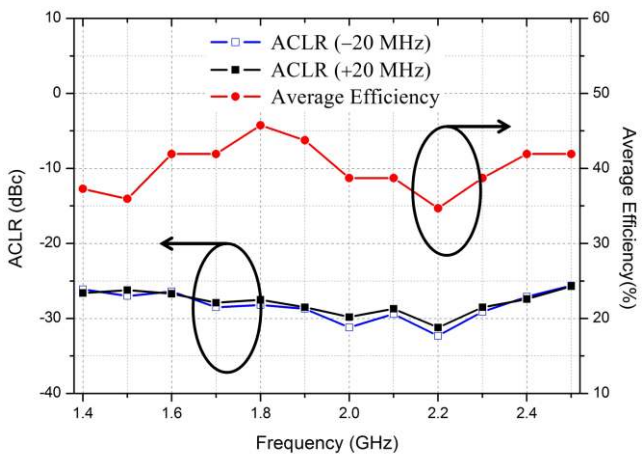

Fig. 17. Measured ACLRs at ±20 MHz offset and DE versus frequency from 1.4 to 2.5 GHz with an average output power about 34.5 dBm.

GHz) are demonstrated in Fig. 15. It can be seen that the 3 dB gain compression points at all four frequencies are over 41.2 dBm, and the fluctuation of the small signal gain between the different frequencies is less than 1.5 dB. For the lower two frequencies, their maximum DEs are higher than 75%, while the peak DEs at the other two frequencies are 69.5% and 68 %, respectively.

The proposed PA was compared with other published broadband PAs, as shown in Table I. Although the proposed design did not provide an operating bandwidth as broad as those in [7], [9], and [15], it is worth noting that those three designs either forfeited second harmonic control or transferred PA modes, leading to a lower DE and a smaller saturated output power. Compared with [10], [13], and [14], the proposed PA exhibited a greater fractional bandwidth with a higher gain, a larger output power, and a higher DE simultaneously. The high performance of the proposed MN can be mainly attributed to its ability to maintain the CCF^{-1} mode over a larger bandwidth, due to its more accurate realization of the theoretical fundamental and the second harmonic impedances.

B. Measurement Results with 20-MHz LTE Signal

To verify the capability of the fabricated PA to linearly amplify modulated signals, a measurement platform is set up that includes a vector signal generator (Keysight E4438C), a spectrum analyzer (Keysight E4445A), and a PC running MATLAB software, as shown in Fig. 16. The baseband signal was first generated in the computer, then up-converted to RF by the E4438C, pre-amplified by a broadband driver, and finally sent to the device under test (DUT). On tshe feedback loop, the output signal of the proposed PA was captured,

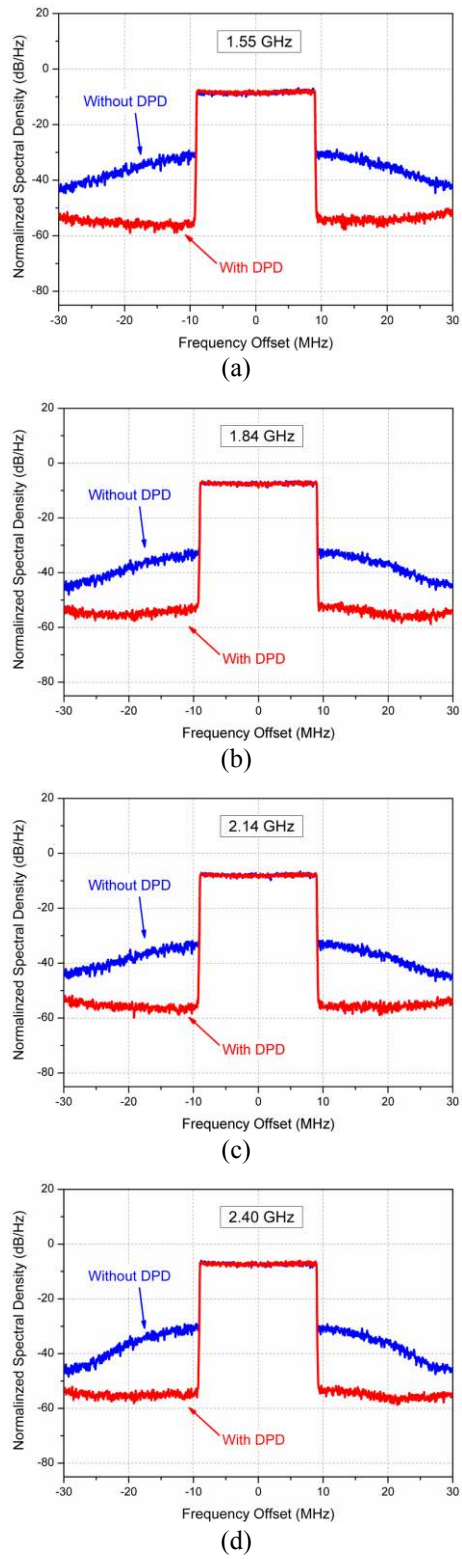

Fig. 18. Measured spectra for a 20 MHz LTE signal with and without DPD at an average output power of approximately 34.5 dBm. (a) at 1.55 GHz. (b) at 1.84 GHz (c) at 2.14 GHz (d) at 2.40 GHz.

TABLE II
Linearity Performance for 20 MHz LTE Signal

Frequency (GHz)		1.55	1.84	2.14	2.40
ACPR (dBc)	Without DPD	-26.5/-26.4	-29.3/-28.7	-28.9/-28.7	-27.4/-27.6
	With DPD	-46.4/-45.2	-47.8/-47.9	-47.3/-47.6	-48.0/-49.0
EVM (%)	Without DPD	15.9	10.9	11.4	13.8
	With DPD	1.5	1.2	1.1	1.1
Output Power (dBm)		34.6	34.5	34.3	34.3
Drain Efficiency (%)		37	45.8	37	42

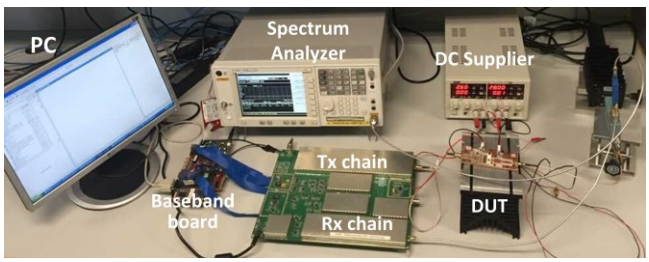

Fig. 19. Linearization platform for 100-MHz dual-band dual-mode signal.

down-converted, and sent to the PC for DPD model extraction and signal processing by the E4445A.

A 20-MHz LTE signal with a peak-to-average power ratio (PAPR) of 7.0 dB was used when the frequency was being swept from 1.4 to 2.5 GHz with a step of 100 MHz. As shown in Fig. 17, the average efficiency (AE) was greater than 35%, up to 46% at 1.8 GHz, with an output power of approximately 34.5 dBm over the band of interest. Besides, the adjacent channel leakage ratio (ACLR) at ±20-MHz offset fluctuated from -26 to -32.5 dBc.

Linearization with DPD was undertaken at 1.55, 1.84, 2.14, and 2.4 GHz with an output power of 34.5 dBm, respectively. Since the AM/AM and AM/PM characteristics of the tested PA showed expansion effects in the low amplitude region but compression effects in the high amplitude region, the piecewise decomposition technique [19] together with the 2nd order dynamic derivation reduction (DDR) DPD technique [20] are employed to build the DPD model. The nonlinear order and memory depth were set as [7, 7] and [5, 5], respectively. The normalized decomposition threshold was set to 0.5. The measured spectrums with and without DPD are displayed in Fig. 18. At all four frequencies, ACLRs without DPD at ±20 MHz offset varied in the range of -26.4 to -29.3 dBc. After linearization, ACLRs were substantially reduced to at least -45.2 dBc, as listed in Table II. Variations of the EVMs at four frequencies before and after DPD are summarized in Table II, revealing the significant improvement of linearity brought by DPD. It is worth noting that AEs in four cases were greater than 37%, up to 45.8% at 1.84 GHz.

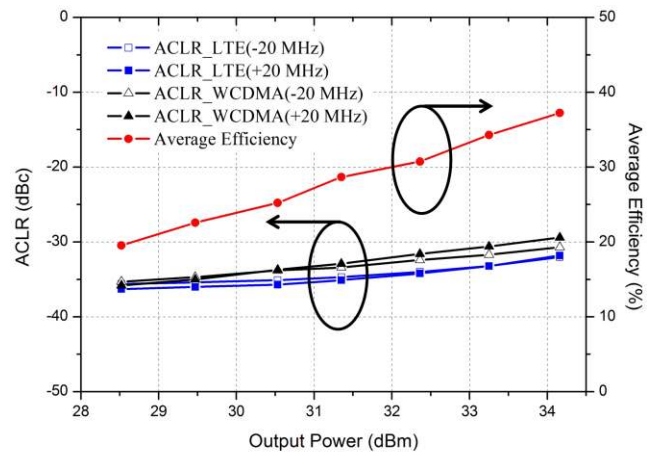

Fig. 20. Measured ACLRs at ±20 MHz offset for both WCDMA and LTE signals and measured average efficiency versus output power at 2.14 GHz.

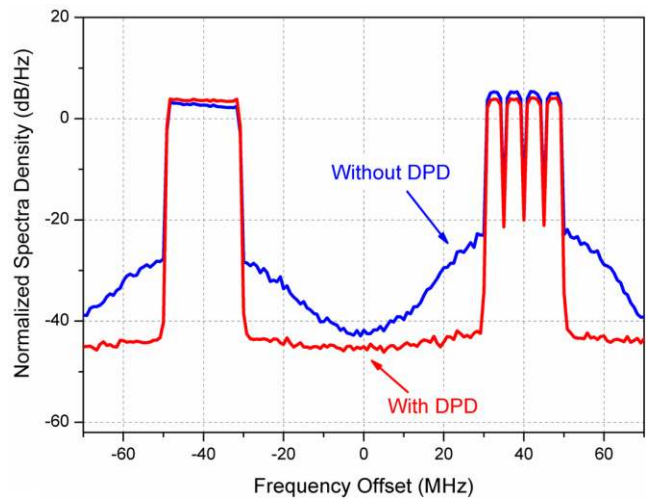

Fig. 21. Measured spectra for the dual-band dual-mode modulated signal with and without DPD at an average output power of 34.2 dBm.

C. Measurement Results with 100-MHz Dual-Band Dual-Mode Signal

To further examine the performance of the implemented PA with linearization, a dual-band dual-mode modulated signal consisting of a 20-MHz four-carrier WCDMA signal and a 20-MHz single-carrier LTE signal with a frequency spacing of 60 MHz and a PAPR of 9.2 dB was utilized for excitation. Since linearization platform in Fig. 16 can't handle such a wideband signal, the following measurements and the DPD validation were conducted in the platform designed in [21], as shown in Fig. 19. On the transmitter chain, the baseband signal source was generated in MATLAB and sent to a baseband board for digital signal processing. Then, an RF board was employed to transform the baseband signal into the analog domain and up-convert to 2.14 GHz with proper power level. Finally, the RF signal was fed to the DUT. On the receiver side, the feedback loop was utilized to capture the output signal of the DUT, down-convert it to the digital baseband, and eventually send it to the PC for further processing. Further

TABLE III
Broadband PAs Comparison with Modulated Signals

Ref	Signal Type	Signal BW (MHz)	AE (%)	BOP* (dBm)	ACLR with DPD (dBc)
[7]	LTE	20	27†	11	-44
[9]	16 QAM	0.3	44	4.5	-32††
[10]	LTE-advanced	100	37.8	7.5	-48
[13]	LTE-advanced	100	30.5	9	-46.0
[14]	LTE	40	46	6.5	-49.7
[15]	WCDMA	5	25.6†	7	-45.5
This Work	LTE	20	45.8	7	-47.9
	Dual-Band Dual-Mode	100	37	7.5	-46.1

* Back-off power.
† Only power-added efficiency was provided.
†† Only ACLR without DPD was provided.

details of the measurement platform can be found in [21]. As the bandwidth of the modulated signal in this case was extended to 100 MHz, the band-limited technique [22] and the piecewise 2nd order DDR model used in the former case were combined here to further optimize the linearization results. The nonlinear order and the memory length were again set to [7, 7] and [5, 5], respectively. The normalized piecewise decomposition threshold was again set to 0.5, and the bandwidth of the band-limited function was set to 140 MHz.

In Fig. 20, the measured ACLRs at ±20 MHz offset and the average efficiency versus output power are displayed. As it can be seen, with the increment of output power from 28.5 to 34.2 dBm, the AE gradually increases to 37%, while ACLRs of both signals at the ±20 MHz offset degrade slowly, falling between -29.4 and -32 dBc without linearization.

Driven by the same signal, the fabricated PA was linearized at 2.14 GHz when supplying an output power of 34.2 dBm and an AE of 37%. In Fig. 21, the ACLRs lower than -46.1 dBc at ±20-MHz offset for both signals can be achieved. Finally, a detailed comparison of the performance of the proposed PA under the stimulus of modulated signals with other existing broadband PAs is given in Table III. In a nutshell, the implemented PA exhibits the potential of to linearly amplify modulated signals under different scenarios with decent efficiency.

V. Conclusion

A broadband highly efficient CCF^{-1} PA with a modified elliptic LPF OMN has been presented in this paper. The necessity of swift transition from the higher end of the fundamental to the lower end of the second harmonic was thoroughly explained from both theoretical and practical points of view. The synthesized design approach of the modified elliptic LPF OMN was demonstrated step-by-step. Measured results of the fabricated PA revealed greater than 68% DE with at least 12.5 W of output power from 1.35 to 2.5 GHz, representing a 60% fractional bandwidth.

Together with DPD, the proposed PA exhibited its capability to linearly amplify a 20 MHz LTE signal with an average efficiency ranging from 35 to 46% at an average output power around 34.5 dBm over the entire band of interest. Stimulated by a dual-band dual-mode modulated signal at 2.14 GHz, the proposed PA generated an average efficiency of 37% at output power of 34.2 dBm while restricting ACLR to below -46.1 dBc.

References

[1] S. C. Cripps, P. J. Tasker, A. L. Clarke, J. Lees, and J. Benedikt, "On the continuity of high efficiency modes in linear RF power amplifiers," *IEEE Microw. Wireless Compon. Lett.*, vol. 19, no. 10, pp. 665-667, Oct. 2009.

[2] P. Wright, J. Lees, J. Benedikt, P. J. Tasker, and S. C. Cripps, "A methodology for realizing high efficiency class-J in a linear and broadband PA," *IEEE Trans. Microw. Theory Techn.*, vol. 57, no. 12, pp. 3196-3204, Dec. 2009.

[3] V. Carrubba, A. L. Clarke, M. Akmal, J. Lees, J. Benedikt, P. J. Tasker, and S. C. Cripps, "The continuous class-F mode power amplifier," in *40th Eur. Microw. Conf.*, Oct. 2010, pp. 1674-1677.

[4] V. Carrubba, A. L. Clarke, M. Akmal, J. Lees, J. Benedikt, P. J. Tasker, and S. C. Cripps, "On the extension of the continuous class-F mode power amplifier," *IEEE Trans. Microw. Theory Techn.*, vol. 59, no. 5, pp. 1294-1303, May 2011.

[5] V. Carrubba, A. L. Clarke, M. Akmal, J. Lees, J. Benedikt, S. C. Cripps, and P. J. Tasker, "Exploring the design space for broadband pas using the novel "continuous inverse class-F mode"," in *41st Eur. Microw. Conf.*, Oct. 2011, pp. 333-336.

[6] V. Carrubba, A. L. Clarke, M. Akmal, J. Lees, J. Benedikt, S. C. Cripps, and P. J. Tasker, "The continuous inverse class-F mode power amplifier with resistive second-harmonic impedance," *IEEE Trans. Microw. Theory Techn.*, vol. 60, no. 6, pp. 1928-1936, Jun. 2012.

[7] P. Saad, C. Fager, H. Cao, H. Zirath, and K. Andersson, "Design of a highly efficient 2-4-GHz octave bandwidth GaN-HEMT power amplifier," *IEEE Trans. Microw. Theory Techn.*, vol. 58, no. 7, pp. 1677-1685, Jul. 2010.

[8] K. Chen and D. Peroulis, "Design of highly efficient broadband class-E power amplifier using synthesized low-pass matching networks," *IEEE Trans. Microw. Theory Techn.*, vol. 59, no. 12, pp. 3162-3173, Dec. 2011.

[9] K. Chen and D. Peroulis, "Design of broadband highly efficient harmonic-tuned power amplifier using in-band continuous class-F^{-1}/F mode transferring," *IEEE Trans. Microw. Theory Techn.*, vol. 60, no. 12, pp. 4107-4116, Dec. 2012.

[10] J. Xia, X. Zhu, and L. Zhang, "A linearized 2-3.5 GHz highly efficient harmonic-tuned power amplifier exploiting stepped-impedance filtering matching network," *IEEE Microw. Wireless Compon. Lett.*, vol. 24, no. 9, pp. 602-604, Sept. 2014.

[11] C. Huang, S. He, F. You, and Z. Hu, "Design of broadband linear and efficient power amplifier for long-term evolution applications," *IEEE Microw. Wireless Compon. Lett.*, vol. 23, no. 12, pp. 653-655, Dec. 2013.

[12] D. Wu, F. Mkadem, and S. Boumaiza, "Design of a broadband and higly efficient 45 W GaN power amplifier via simplified real frequency techniques," in *IEEE MTT-S Int. Microw. Symp. Dig.*, Jun. 2010, pp. 1090-1093.

[13] Y. Sun and X. Zhu, "Broadband continuous class-F^{-1} amplifier with modified harmonic-controlled network for advanced long term evolution application," *IEEE Microw. Wireless Compon. Lett.*, vol. 25, no. 4, pp. 250-252, Apr. 2015.

[14] N. Tuffy, L. Guan, A. Zhu, and T. Brazil, "A simplified broadband design methodology for linearized high-efficiency continuous class-F power amplifiers," *IEEE Trans. Microw. Theory Techn.*, vol. 60, no. 6, pp. 1952-1963, Jun. 2012.

[15] Z. Dai, S. He, F. You, J. Peng, P. Chen, and L. Dong, "A new distributed parameter broadband matching method for power amplifier via real frequency technique," *IEEE Trans. Microw. Theory Techn.*, vol. 63, no. 2, pp. 449-458, Feb. 2015.

[16] D. M. Pozar, *Microstrip Engineering.* 3rd ed. Boston, MA: Wiley, 2005.

[17] P. J. Tasker and J. Benedikt, "Waveform inspired models and the harmonic balance emulator," *IEEE Microw. Mag.*, vol. 12, no. 2, pp. 38-54, Apr. 2011.

[18] J. S. Hong, and M. J. Lancaster, *Microstrip Filters for RF/Microwave Applications.* New York: Wiley, 2001.
[19] A. Zhu, P. J. Draxler, C. Hsia, T. J. Brazil, D. F. Kimball, and P. M. Asbeck, "Digital predistortion for envelope-tracking power amplifiers using decomposed piecewise Volterra series," *IEEE Trans. Microw Theory Techn.*, vol. 56, no. 10, pp. 2237-2247, Oct. 2008
[20] L. Guan and A. Zhu, "Simplified dynamic deviation reduction-based Volterra model for Doherty power amplifiers," in *Proc. IEEE Int. Integer. Nonlinear Microw. Millimeter-Wave Circuits Workshop,* Vienna, Austria, Apr. 2011, pp.1-4.
[21] L. Guan, R. Kearney, C. Yu and A. Zhu, "High performance digital predistortion test platform development for wideband RF power amplifieters," *Int. J. Microw. Wireless Tech*., vol. 5, no. 2, pp. 149-162, Apr. 2013.
[22] C. Yu, L. Guan and A. Zhu, "Band-limited Volterra series-based digital predistortion for RF power amplifiers", *IEEE Trans. Microw Theory Techn.*, vol. 60, no. 12, pp. 4198-4208, Dec. 2012.

Mengsu Yang received the B.E. degree in information engineering and M.E. degree in electromagnetic fields and microwave technology from Southeast University (SEU), Nanjing, China, in 2008 and 2012, respectively. He is currently working toward the Ph.D degree at University College Dublin (UCD), Dublin, Ireland.

He is currently with the RF and Microwave Research Group, UCD. His research interests mainly focus on the design of high-efficiency, broadband power amplifiers (PAs).

Jing Xia (S'12-M'15) received the M.E. degree in computer science and technology from Jiangsu University, Jiangsu, China, in 2007, and the Ph.D. degree in electromagnetic field and microwave technology from Southeast University, Nanjing, China, in 2014.

From 2015 to 2016, he was a Post-Doctoral Research Fellow in the RF and Microwave Research Group, University College Dublin (UCD), Dublin, Ireland. His recent research is focused on high back-off efficiency power amplifier (PA) design, wideband efficient PA design, and digital pre-distortion techniques.

Yan Guo (S'13) received the B.E. degree in information science and engineering from East China Jiaotong University, Nanchang, Jiangxi Province, China, in 2007, the M.E. degree in communication and information systems from Southeast University, Nanjing, China, in 2011, and the Ph.D degree in electronic engineering from University College Dublin (UCD), Dublin, Ireland.

He is currently a Post-Doctoral Research Fellow in the RF and Microwave Research Group, UCD. His research interests include digital predistortion for RF power amplifiers and RF digital to analog converter (RFDAC), and related field-programmable gate-array (FPGA) hardware implementation.

Anding Zhu (S'00-M'04-SM'12) received the B.E. degree in telecommunication engineering from North China Electric Power University, Baoding, China, in 1997, the M.E. degree in computer applications from the Beijing University of Posts and Telecommunications, Beijing, China, in 2000, and the Ph.D degree in electronic engineering from University College Dublin (UCD), Dublin, Ireland, 2004.

He is currently a Senior Lecturer with the School of Electrical and Electronic Engineering, UCD. His research interests include high-frequency nonlinear system modeling and device characterization techniques with a particular emphasis on behavioral modeling and linearization for RF power amplifiers (PAs). He is also interested in wireless and RF system design, digital signal processing, and nonlinear system identification algorithms.